Describing seasonal mixtures of cloud regimes via "regimes of regimes"

Nayeong Cho[a,b], Lazaros Oreopoulos[b], Dongmin Lee[c,b], Jackson Tan[a,b] and Daeho Jin[a,b]

a University of Maryland Baltimore County, Baltimore, Maryland

b Earth Sciences Division, NASA's Goddard Space Flight Center, Greenbelt, Maryland

c Morgan State University, Baltimore, Maryland

Corresponding author: Lazaros Oreopoulos, Lazaros.Oreopoulos@nasa.gov

ABSTRACT

We propose a new type of cloud classification, relevant to monthly or longer time scales, but which inherently still encompasses cloud subgrid variability information at ~100 km scales. Our proposed classification partitions frequencies of occurrence over these scales of previously defined cloud regimes (CRs). We call the resulting distinct cloud entities regimes of regimes (RORs). While the CRs have been previously shown to successfully classify daily mesoscale subgrid variability via distributions of cloud fraction within distinct combinations of cloud top pressure and cloud optical thickness, the RORs essentially represent the prevalent seasonal mixtures of these CRs. RORs thus embody the seasonal cloudiness of a mesoscale region. We show that each ROR can still be associated with more traditional cloud classifications via composites of coincident active (lidar and cloud radar) cloud views. In a first application that gauges the potential utility of RORs, we pair them with CERES EBAF radiative fluxes to gain insight into recent trends of the cloud radiative effect. The ROR corresponding to an environment of shallow convection stands out in this analysis largely because of its declining population. Our study demonstrates the potential of RORs to categorize globally mesoscale cloudiness at monthly/seasonal scales and to serve as proxies of different atmospheric states at these scales.

1. Introduction

While the general features of the geographical distribution of cloudiness can be consistently described in broad terms, i.e., "low" clouds occurring in subtropical marine regions of atmospheric subsidence, deep convection occurring in the narrow geographical zone with the strongest upward vertical motion known as the ITCZ, etc. (e.g., Fig. 7.4 in Boucher et al. 2013), such vague, non-rigorous descriptions often lack consistency, which limits their value. Defining cloud types from either passive or active satellite observations (Welch et al. 1992; Bankert 1994; Rossow and Schiffer 1999; Wang and Sassen 2001; Ceccaldi et al. 2013) is also somewhat arbitrary, having only an approximate correspondence to the standard WMO cloud classification (WMO, 1956) traditionally used by surface observers. Furthermore, it is often unclear what spatiotemporal range of scales are appropriate for classifications based on satellite-derived cloud properties (Koren et al. 2008, Wood and Field 2011). Are they meaningful only for instantaneous observations within the instrument's footprint, larger spatial scales that encompass multiple instantaneous footprints, or multiple footprints across larger areas and over a certain time span? It is not uncommon for the spatial persistence (coherence) of a particular cloud type to be weak, since a mesoscale area of ~100 km comprising many instrument footprints can conceivably contain at any instance multiple cloud types defined at the footprint level. Consider then the cloudiness in this mesoscale area over a month, and even more cloud type diversity will be encountered. How to characterize cloudiness at monthly or longer scales at such mesoscale regions becomes then a conundrum. Distributions obtained from grid-level spatial averages of instantaneous cloud properties are narrower and conceal the true nature of cloudiness we seek to classify. Preservation of cloud variability at the original spatial scale of the instantaneous observation should perhaps then become a consideration in cloud classification schemes.

Cloud regimes (CRs), aka Weather States (WSs) (Jakob and Tselioudis 2003; Rossow et al. 2005; Tselioudis et al. 2013; Oreopoulos et al. 2014, Oreopoulos et al. 2016; Cho et al. 2021), have been previously introduced as a convenient and arguably physically meaningful approach to achieve cloud classification of mixtures of different cloud types that mitigates the loss of information resulting from homogenization due to spatial averaging. Based on daily or three-hourly joint histograms describing the frequency of occurrence of discrete pixel-level cloud top pressure (CTP) and cloud optical thickness (COT) combinations during sunlit hours, where each combination can be viewed as a "cloud type", cloud regimes provide a

compact way to describe semi-instantaneous cloud subgrid variability at mesoscales. Using however distributions of cloud properties retrieved at the pixel-level scale for cloud classifications presents its own challenges. Instead of the narrowing effect on distributions of grid-level averaging, the pixel-level cloudy property distributions become broader as temporal scales expand. If one were to construct, for example pixel-level CTP-COT joint histograms over increasingly longer time scales and/or larger spatial scales, they would become progressively more featureless (more likely to be devoid of distinct frequency peaks) the longer the sampling period and the larger the domain, rendering themselves once again unsuitable for cloud grouping and classification. In short, when using cloud property distributions for cloud classification, the specific spatiotemporal scales chosen to build them also matter.

Motivated by this state of affairs, in this work we pay attention to the temporal aspect of cloud classification and investigate whether we can overcome the inherent obstacle of spatial distributions becoming progressively more featureless the longer the sampling time scale. We specifically investigate whether a meaningful cloud classification at monthly or longer time periods that preserves information about instantaneous subgrid variability at mesoscales is possible. In essence, we seek an effective way to bypass the undesired smoothing and loss of information that characterizes temporal distributions of grid-average values, while also avoiding the loss of distinct features that accompanies the expansion of the reference period over which pixel-level distributions are built. We make the case that a new concept of cloud classification we call “regimes of regimes” (RORs) avoids both pitfalls and can serve as a useful descriptor of seasonal cloudiness at mesoscales. We accordingly introduce new cloud classes representing CR mixtures that tend to re-occur over staggered 3-month periods. The paper’s main goal is then to examine whether RORs are indeed a physically appropriate and viable concept that can serve as a novel climatological description of the planet’s cloudiness.

In the remainder of the paper, we detail the derivation of RORs, provide their physical interpretation, and explore their potential utility for understanding not only the mean state of cloud radiative effects, but also their recent trends and implied short-term feedbacks.

2. ROR Derivation

The RORs of this study are derived from the 1° daily MODIS CR dataset of Cho et al. (2021). The salient characteristics of these CRs are expressed via: (1) their centroids, namely

mean joint histograms of the clusters representing the CRs obtained from applying a clustering algorithm on MODIS daytime 1° CTP-COT joint histograms, described in Cho et al (2021); and (2) the multi-year mean maps of CR relative frequency of occurrence (RFO) over a 20-year period obtained from assigning a CR daily to each grid cell. These CR centroids and RFO maps are shown in Fig. 1. To obtain RORs, we built histograms of CR normalized frequency of occurrence (FOC, per the terminology of Tselioudis and Rossow 2011), over "rolling" 3-month periods for all one-degree grid cells containing CRs (Fig. 2), essentially a 12-element vector of the grid cell's seasonal RFO. For example, a CR FOC histogram for January-February-March is followed by a February-March-April histogram, which is then followed by one for March-April-May, and so forth. The FOC histogram is nominally assigned to the middle month of the 3-month period. Such overlapping 3-month windows are employed to achieve big enough sample sizes that suppress the noise of 1° histograms. CRs derived from both morning (Terra satellite) and afternoon (Aqua satellite) MODIS cloud data enter the construction of these histograms, so each of them is built from 3 (month) × ~30 (days per month) × 2 (Terra and Aqua) ≈ 180 values. An example of such a FOC histogram is shown in Fig. 2.

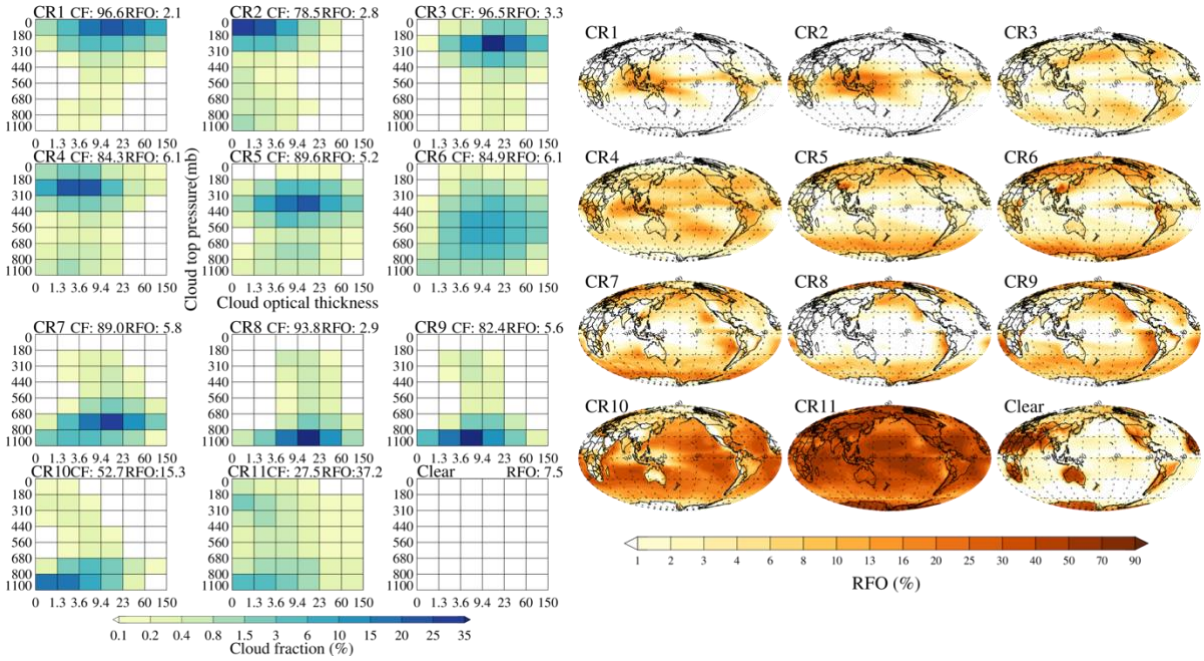

Fig. 1. Centroids (cluster mean joint histograms from *k*-means clustering, left) and maps of mean relative frequency of occurrence (RFO) of the 1° daily MODIS CRs of Cho et al. (2021).

A large number of CR FOC histograms (~15M) such as the one in Fig. 2 were furnished to a k-means clustering algorithm. While objective criteria exist to determine the number of

clusters that optimize centroid distinctiveness (McDonald et al. 2016; Schuddeboom et al. 2018; Jin et al. 2021), our experience from previous implementations of k-means in cloud classification exercises suggests that such algorithmically derived "optimal" numbers yield clusters that are too correlated geographically to be considered physically distinct. We thus follow again our previous practice of settling on the desired number clusters by trial and error based on visual inspection and judicial assessment of the output. Using such an empirical approach, we settled on K=8 as the "best" number of clusters to compactly describe the planet's cloudiness in terms of seasonal one-degree RORs. While a larger number would theoretically provide a better separability of centroids, in practice we noticed that the algorithm does not actually split the clusters that would apparently benefit the most, i.e., those with somewhat excessive CR mixing. Another possible avenue to improve cluster separation, namely performing additional clustering only on the histograms of the clusters deemed too mixed, was not attempted at this time because more (albeit presumably better separated) clusters undermine the practical utility of RORs when employed in subsequent analyses. Staying with K=8 has also the additional benefit of no extreme disparities in ROR global occurrences: global ROR RFOs range between ~7% and ~20% indicating that no ROR is exceedingly rare or overly frequent. While RORs can arguably be refined in future efforts, the present set satisfies our first order goal to demonstrate the physical foundation and viability of the concept.

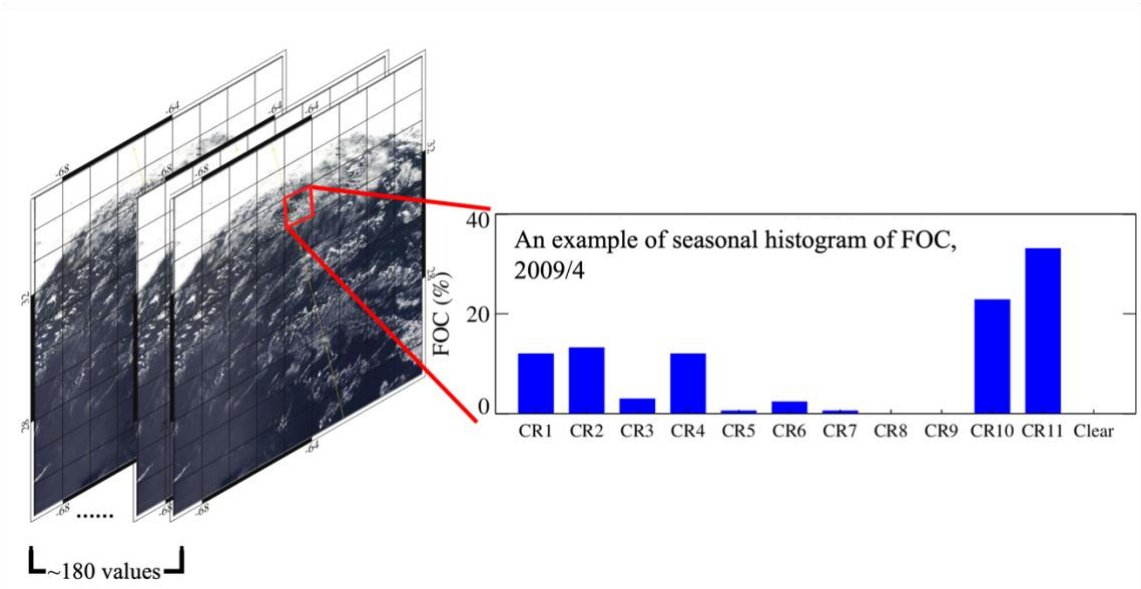

Fig. 2. Illustration of a seasonal (3-month) histogram of CR normalized FOC (Terra and Aqua) in a 1° grid cell. ~15M of such histograms are clustered to produce RORs, with each histogram constructed from ~180 values.

It should be noted that the seeds of an ROR-like concept were previously planted by Tselioudis and Rossow (2011). In that work their entities represented nearly instantaneous tropical WS mixtures based on FOC histograms built daily at large spatial scales of 30°×30°. Hence, fundamental differences with the current work are that the WS FOC histograms of Tselioudis and Rossow (2011) reflect variations in much larger domains than mesoscale, and at semi-instantaneous rather than seasonal temporal scales. Hence the physical meaning of their cloud mixtures is quite different than ours, as they capture the fast propagation of expansive features of the tropical circulation through the prism of WS snapshots covering very large areas. Our RORs on the other hand showcase the seasonal variability of persistent cloud mixtures at mesoscales.

3. ROR definitions and characteristics

In order to come up with a physical interpretation of the RORs we examined their centroids as obtained from the *k*-means clustering procedure, monthly "snapshot" maps of their dominant geographical location, the statistics of geographical occurrences over the 20 × 12 = 240 months of our dataset, composites of cloud features derived from a fundamentally distinct type of (coincident) space-based observations, namely active lidar and radar observations, and the prevailing dynamical environment, as expressed by large-scale mid-tropospheric vertical velocity, in which RORs are embedded. All these aspects of RORs are presented in this section.

a. ROR centroids

Centroids, i.e., mean CR FOC histograms assigned to each cluster by the clustering process provide the first clues on the nature of the RORs (Fig. 3). Our visualization of the ROR centroids as horizontal "mosaic" bars shows both the normalized FOC of each CR within an ROR (via the numbers displayed), but perhaps most appropriately, how the FOC within an ROR differs from the CR's global RFO (via the colors, where blue hues correspond to values below and red hues to values above the CR's global RFO; the deeper the colors the larger the deviation from global RFOs). Next to the horizontal bars we provide: (1) the ROR's global cloud fraction (CF) obtained from globally averaging (using cosine latitude as weight) the CF of successful MODIS daytime cloud retrievals of each grid cell whose CR belongs to the ROR occurrence; and (2) the ROR's global RFO obtained by normalizing the

number of specific ROR occurrences by the total number of all RORs encountered in our dataset, and then weighting by cosine of latitude.

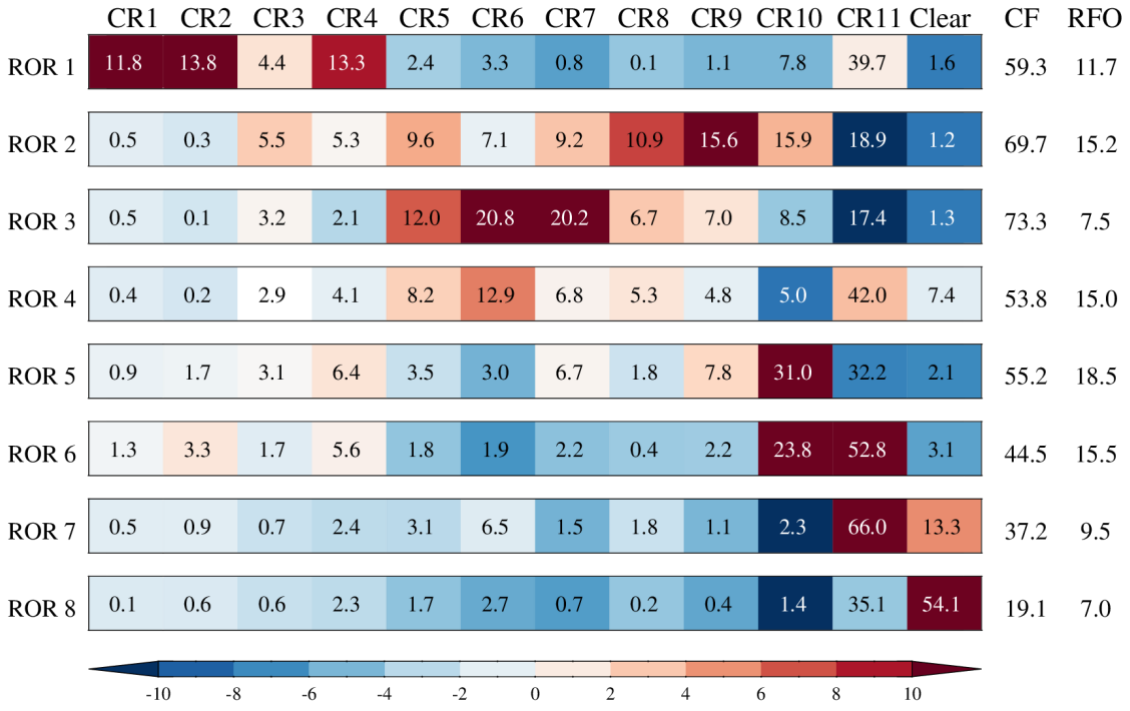

Fig. 3. Centroids (mean CR FOC histograms from *k*-means clustering) corresponding to the RORs, shown as "mosaic" bars where each mosaic "piece" corresponds to a CR. The centroids are represented both by numbers showing the normalized FOC (adding to 100%) of each CR in the ROR's CR mixture, and colors capturing the FOC deviation within the ROR from the CR's global RFO, as explained in the text.

b. Snapshots of ROR geographical occurrence

For each 1° grid cell, the 3-month CR FOC histogram (which, as mentioned previously, can be thought as a 12-element array), nominally attributed to the middle month, is assigned to the ROR whose centroid produces the minimum Euclidean distance from the grid cell's array. Ultimately, an ROR is assigned to each grid cell for every month, with the end result of this action being an "instantaneous" monthly snapshot map, as in Fig. 4. Our 20-year dataset yields 240 such maps available for download at https://doi.org/10.5281/zenodo.11061757, which can also be viewed in succession as an animation (available in the Supplemental Material SM) to gauge ROR seasonal and year-to-year movements. The example map of Fig. 4, for April 2009 (from assignment of March-April-May 2009 CR FOC histograms) as well as the SM's animation loop of the entire dataset supports the notion that the ROR concept has an underlying physical foundation of : RORs are generally organized geographically into large contiguous areas that reveal the climatological distribution of cloud systems with

discerning characteristics on a planetary scale. For this specific month, we note the following: The most convective cloud systems (ROR1) are limited to the tropics and occupy large parts of the ITCZ and SPCZ, and are surrounded by the low broken cloud tropical and subtropical shallow convection of ROR5 and ROR6. The NH land masses are blanketed by ROR4 which contains many weather-producing mid-level clouds, while the midlatitude oceans are dominated by ROR2 which contains stratiform clouds, including the marine stratocumulus not belonging to ROR5. ROR3 is encountered mostly at high latitudes, being quite prominent in the far southern oceans surrounding Antarctica, but also in the northern Atlantic south of Greenland. The low cloud fraction ROR7 does not appear to be too frequent in this season, and besides polar and regions of high relief, has also presence in oceanic tropical areas of sparse cloudiness. Finally, the semi-clear ROR8 is associated with deserts and other areas where low humidity may exhibit seasonal variations.

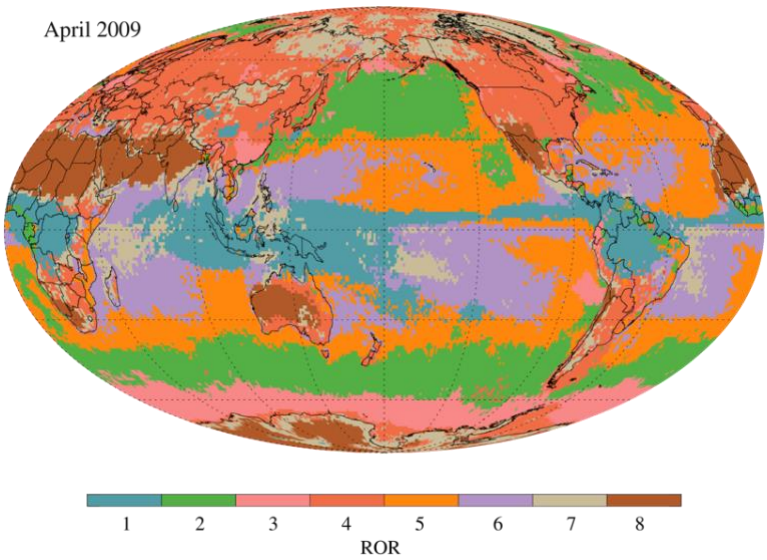

Fig. 4. Snapshot map of ROR assignment of 3-month CR FOC histograms for March-April-May 2009 (nominally assigned to April 2009).

c. Maps of ROR RFOs

In addition to global RFO and monthly snapshot maps of ROR occurrence, we can also examine the multi-annual average geographical prevalence of RORs. Geographical distributions of RFO can be created by counting for each grid cell the fraction of the time an ROR occurs over the 240-month period. The resulting ROR RFO maps (normalized counts of ROR occurrence) are shown in Fig. 5. These maps clearly show that the RORs generally

exhibit coherent and rather contiguous geographical distributions, broadly consistent with the descriptions we provided above for April 2009.

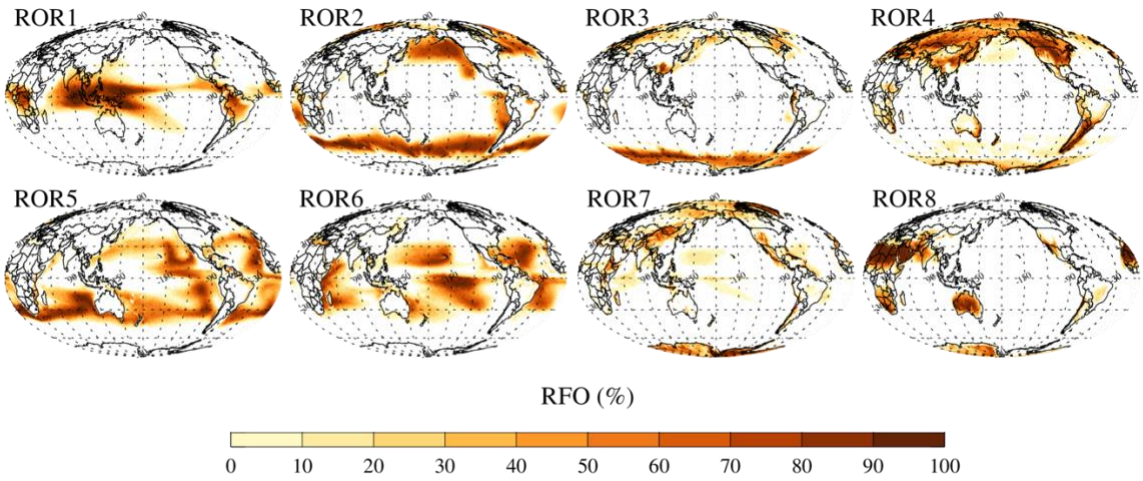

Fig. 5. Multi-annual (20 years) maps of ROR RFO obtained by counting monthly ROR occurrences over the analysis period in each 1° grid cell and normalizing by the total number of ROR occurrences (nominally 240) in the grid cell.

d. ROR interpretation

Additional insight on RORs can be gained by constructing distributions of mid-tropospheric 500 hPa large-scale vertical velocity ("omega") from coincident MERRA-2 monthly reanalysis values. This reanalysis assimilates modern satellite observations not available to its predecessor, MERRA, and includes updates to the Goddard Earth Observing System (GEOS) model and analysis scheme (Gelaro et al. 2017). The omega distributions corresponding to each ROR are visualized via their quartile values in the form of a boxplot in Fig 6. The dynamical environment revealed by this figure, along with the previously shown CR FOCs within ROR centroids, global CFs and RFOs, snapshot maps, and geographical distribution of ROR RFOs provide quite a comprehensive picture on the nature of the RORs which we can now summarize as follows:

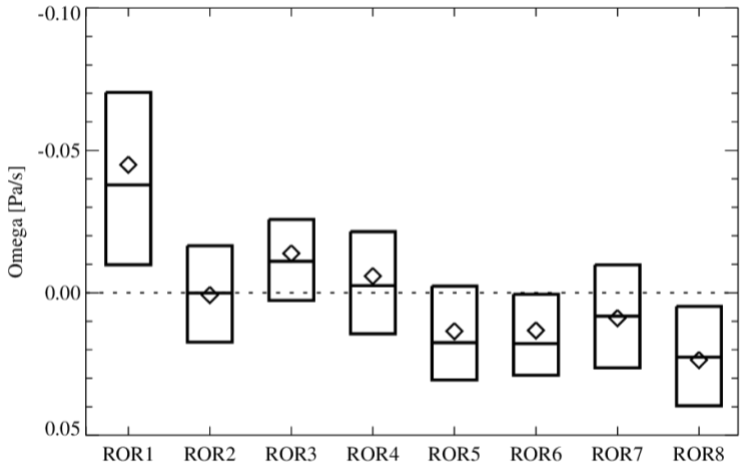

Fig. 6. Mean (diamonds), median (horizontal lines), and interquartile range of large-scale 500 hPa vertical velocity distributions (boxes) constructed by matching monthly MERRA-2 values with ROR occurrences for our entire 20-year dataset. Negative values indicate large scale ascent while positive value large scale descent.

- Made of anomalously high amounts of CR1(tropical deep convection) and CR2 (tropical anvils and cirrus), but also CR3 (tropical and midlatitude convection) and CR4 (midlatitude and subtropical high clouds), ROR1 contains by far the highest proportion of high and deep clouds and is the rarest of the seven RORs with substantial average cloud fractions. Given the prevalence of CR1 and CR2, ROR1 unsurprisingly occurs in an environment of strong ascent (Fig. 6). It is the most tropical of all RORs with large presence primarily in the tropical western Pacific and secondarily over tropical Africa and South America, reflecting the mean annual position of the ITCZ. Monthly ROR snapshot maps examined either individually or as an animation (available in the SM or at https://doi.org/10.5281/zenodo.11061757) show that the buildup and decay of the Indian monsoon can be tracked via ROR1. Moreover, ENSO signals can also be gleaned through ROR1: for example, comparing the July ROR occurrence map of 2015 (strong El Niño initiated earlier that year) with the July map of 2010 (strong La Niña initiated earlier that year), clearly shows the anomalous 2015 expansion of deep convection represented by ROR1 into the eastern tropical Pacific.

- ROR2 has large mean CF and encompasses CR8 (thick low stratus) and CR9 (oceanic stratocumulus) at rates substantially above climatology, with the former representing thick low stratus and the latter mostly marine stratocumulus. ROR2's RFO map consequently shows extensive coverage at both the subtropics and mid-latitudes, with the latter regions likely contributing to the above climatology occurrence of storminess via

CR3 and CR5 (high-latitude storms). The extratropical branch of ROR2 is likely where ascending motion primarily occurs, while the subtropical sector contributes to the downward motions seen in Fig. 6's boxplot.

- Occurring mostly at high latitudes, ROR3 is notable for its large mean CF and high relative contributions from CR6 (high-latitude midlevel clouds) and CR7 (thick high stratus) which represent the bulk of mid-level clouds and the highest and thickest of stratus, respectively. Fig. 6 indicates that this ROR occurs in regions of persistent large-scale ascent.

- ROR4 is the most continental of the RORs, but also has substantial polar presence. It is characterized by an excess of mid-level clouds (CR5 and CR6) that can occur in the presence of either upward or downward large-scale motion.

- Being the most frequent of all RORs, ROR5 also stands out as the ROR with anomalously high contributions from CR10 (shallow oceanic convection) and anomalously low contributions from CR11 (low cloud fraction regime). While these two CRs have the lowest cloud fraction, they nevertheless differ substantially with CR10 having nearly double the CF (~53% vs ~27%), allowing ROR5 to still have a considerably large mean CF representing mostly shallow oceanic convection. This interpretation is consistent with prominent presence further away from the west coast of the major continents, with the exception of Australia where marine stratocumulus are of more broken nature. The shallow nature of ROR5 clouds is consistent with subsidence prevailing in their subtropical environment.

- In contrast to ROR5, ROR6 receives anomalously high contributions from both CR10 and CR11 indicating dominant presence of broken clouds that are mixtures of both active shallow convection and also suppressed conditions of fair weather (predominantly downward large-scale motion in Fig. 6) in tropical and subtropical latitudes.

- ROR7 is made up chiefly from CR11 which is the CR of lowest CF associated with dry conditions in the poles and mountainous areas. The upward motions seen in its omega distribution probably come from the low latitudes where this ROR occasionally occurs.

- ROR8 is a semi-clear ROR containing large amounts of completely clear grid cells (CR12) and thus has by far the lowest cloud fraction of all RORs. It is almost always

associated with large-scale descent occurring over deserts, polar regions, and (presumably the leeward side of) mountains.

e. Seasonal Variability

Although no immediate association with the nature of cloudiness represented by each ROR can be made by itself, an examination of the mean annual cycle of ROR RFO and CF provides a compact view of the characteristics of their seasonal variability in terms of the timing of maxima/minima and the magnitude of within-year variations. Figure 7 shows the 20-year-mean annual cycle of ROR CF, when the ROR occurs (top), and of ROR RFO (bottom). One can immediately see that the annual cycles of CF and RFO are generally distinct from each other. The convention of plotting the annual cycle as normalized values with respect to the January multi-annual mean provides the cleanest visualization and conveniently reveals whether January is a (near) minimum value month (i.e., mostly positive deviations occurring for the other months) or a (near) maximum value month (mostly negative deviations occurring for the other months). The biggest CF annual cycle is exhibited by ROR8, the ROR with the smallest cloud amount (~19% annual mean value), with the minimum dropping to ~16 % in the boreal summer months. This is the time of the year when ROR4 RFO nearly doubles, which seems to be associated (according to the time lapse of ROR occurrence in the SM) with a northward expansion of cloudiness over the NH continents and polar regions, as also seen in the seasonal cycles of CR5 and CR6 in Fig. 5 of Cho et al. (2021). The seasonal variabilities of the other RORs are less pronounced, with perhaps ROR3 deserving some attention given its January peak of both RFO and CF. The seasonal cycle of ROR3 seems to be dominated by its Southern Ocean branch, and reflects the peak in thick stratiform cloudiness in the summer months, consistent with the peak in CR7 DJF RFO in Fig. 5 of Cho et al. (2021).

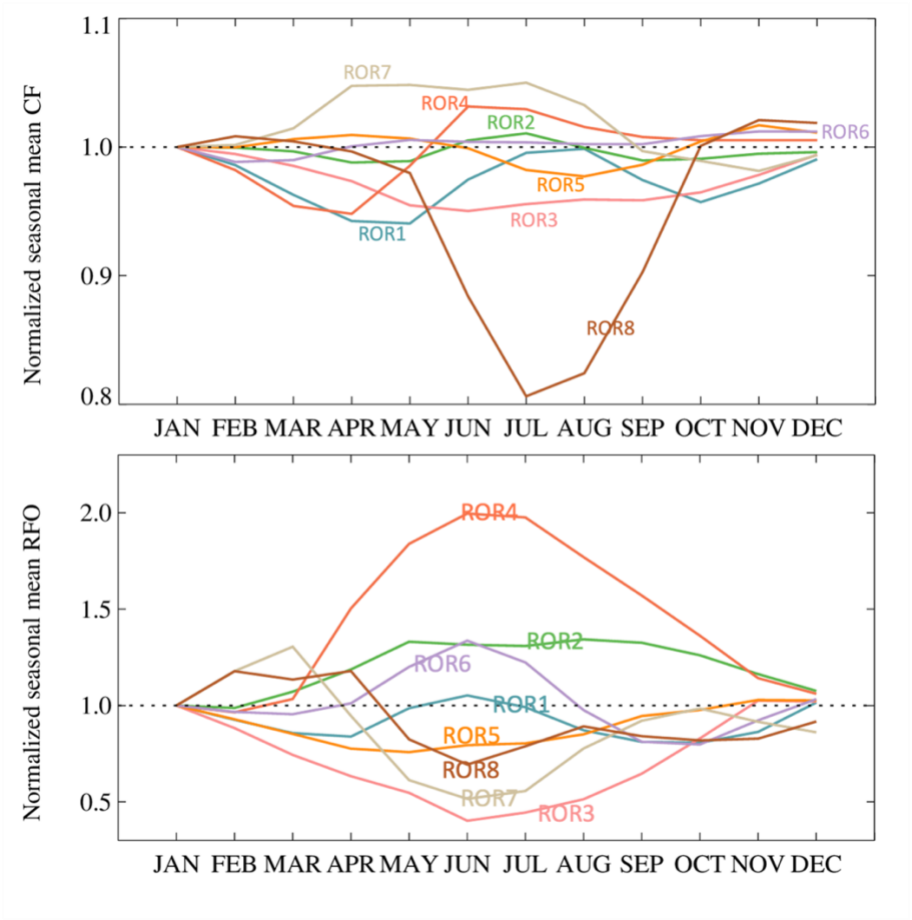

304

305 Fig. 7. The mean seasonal cycle of ROR CF (top panel) and RFO (bottom panel) cycle
306 normalized to multi-annual January values.

307 *f. Active views*

308 It has been previously shown (e.g., Cho et al. 2021) that cloud products from active
309 observations taken contemporaneously within grid cells occupied by CRs can be used to
310 examine their vertical structure as well as their constitution in terms of cloud types
311 originating from an independent classification that exploits the unique capabilities of active
312 observations. The same probing can also be done on RORs, the only material difference
313 being that the compositing of active cloud products is performed over a three-month period.

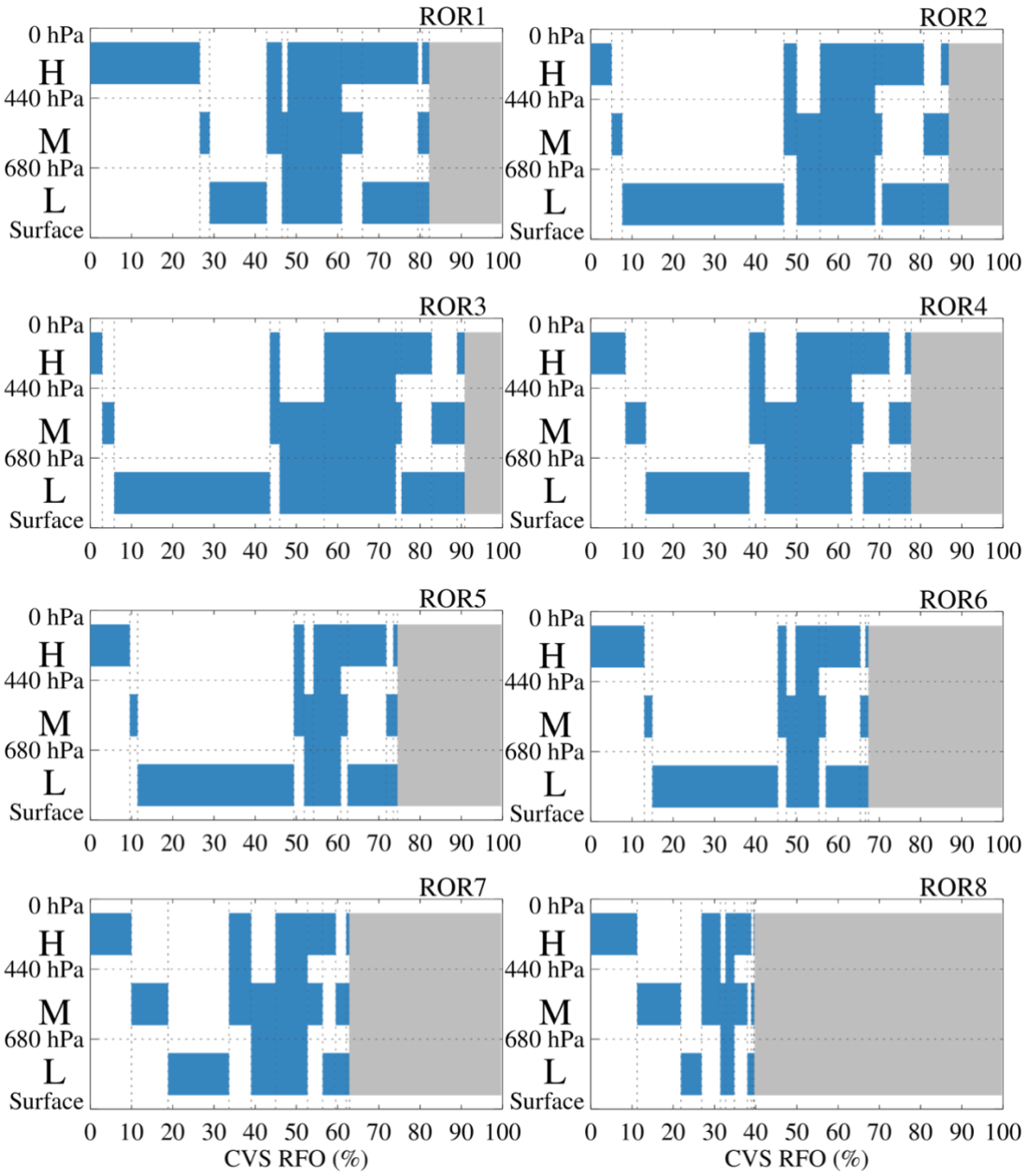

Fig. 8. Cloud Vertical Structure (CVS) composites for each ROR for the period 2007-2020. All panels have the same CVS ordering, with the bar width indicating the relative contribution of each CVS to the ROR. The CVSs were derived by applying the algorithm of Oreopoulos et al. (2017) on the 2BCL R05 Cloudsat dataset.

Figure 8 shows the makeup of each of each ROR in terms of the 10 Cloud Vertical Structures (CVSs, 11 with clear skies) introduced by Oreopoulos et al. (2017). The CVS dataset used here is similarly based to the 2B-CLDCLASS-LIDAR (2BCL) dataset (Sassen et al. 2008), but updated to reflect the most recent Release 5 (R05) version of the dataset, and was expanded to cover more years (14 years, 2007-2020). 2BCL combines CloudSat Cloud Precipitation Radar (CPR) and CALIPSO (CALIOP) lidar measurements and takes advantage of the different sensitivity to hydrometeor type of the two instruments to detect cloud phase

and classify clouds at various layers into different types. The fact that the CloudSat sampling strategy varies throughout this period and becomes daytime-only after 2010 is immaterial for our purposes since CRs and RORs are also daytime-only datasets. In the Fig. 8 visualization the 10 CVS classes are represented by blocks in three broad tropospheric vertical layers (segments) where low (*L*), middle (*M*) and high (*H*) clouds reside, delineated per ISCCP convention by 680 hPa and 440 hPa atmospheric pressure boundaries (Rossow and Schiffer 1999). Blocks can appear in either one, two, or all three of these segments. When present in more than one segment, clouds can occupy the segments either contiguously (indicated as connected) or non-contiguously (separated blocks). The horizontal width of the block indicates the percent contribution of each CVS class to the ROR.

Figure 8 provides the following insights: ROR2, ROR3, and ROR5 all have large amounts of isolated low clouds, indicative of either isolated cumulus clouds or stratocumulus fields. But ROR1, ROR2, and ROR3 also contain high proportions of vertically developed clouds connected across all three segments suggestive of a deep convective nature. ROR4 also comprises appreciable amounts of vertically developed clouds given the second largest (after ROR3) combined proportion of vertically connected clouds spanning either all three or the low and middle segments (the latter suggestive of congestus and cyclonic clouds). The largest by far proportion of stand-alone high clouds is found in tropical ROR1, many of which are likely cirrus outflows associated with deep convention. ROR8 has the lowest cloud fractions of all RORs, but even so it has clouds ~40% of the time on average according to active observations which (on the lidar side) are more sensitive to thin clouds, the largest proportion of which is high clouds, consistent with its prevalence in arid environments.

Comparing the CVSs of these RORs to the CVSs of the CRs (Cho et al. 2021), there is less CVS distinction between the RORs than between the CRs, which is simply a reflection of the fact that the RORs are seasonal aggregations and thus contain a more diverse mixture of cloud types. Nevertheless, the fact that the CVS composition of the RORs exhibits distinct patterns and contrasts (e.g., the amount of isolated high clouds in ROR1 and ROR3) is a testament of the inherent ability of RORs to identify different seasonal cloud conditions.

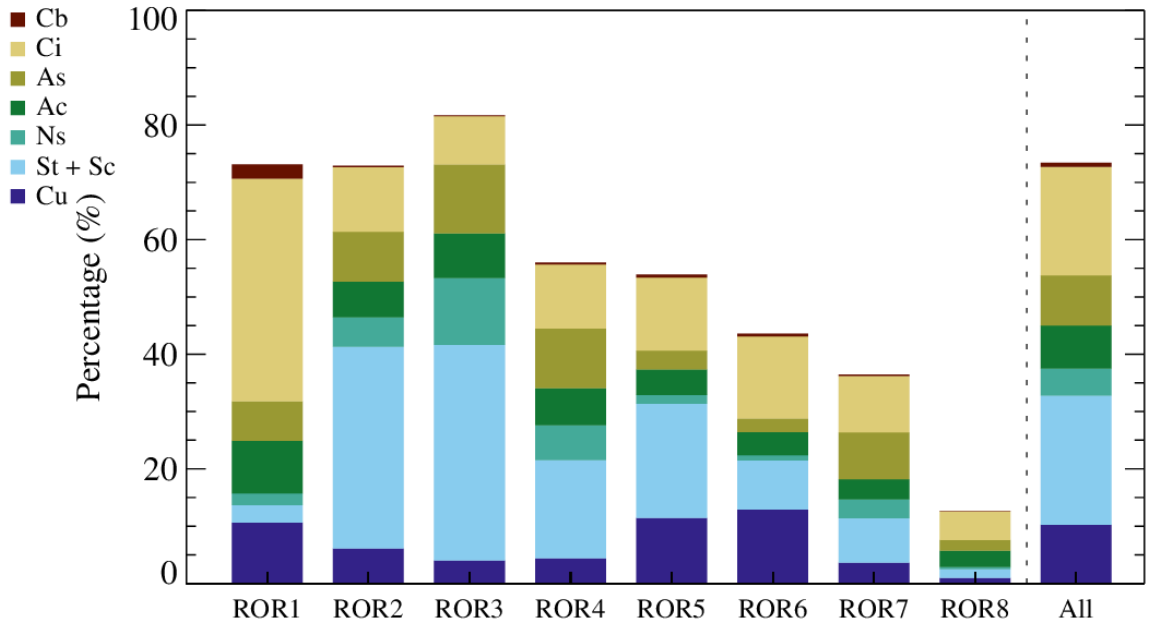

Fig. 9. CloudSat-CALIPSO cloud type occurrence for each ROR created by accumulating 2BCL cloud type occurrences for the 3-month periods used for ROR assignment in one-degree grid cells. The cloud type occurrences were normalized to add to the total cloud fraction for each ROR according to the coincident active observations. Cb = cumulonimbus (deep convection), Ci = cirrus (may also contain cirrocumulus and cirrostratus), As = altostratus, Ac = altocumulus, Ns = nimbostratus, St = stratus, Sc = stratocumulus, and Cu = cumulus (represents cumulus congestus and fair weather cumulus). The last bar shows the global cloud type distribution per 2BCL regardless of ROR.

The 2BCL dataset also contains one or more cloud "types" identified within a "ray" of coincident CALIOP and CPR observations (Sassen et al. 2008). We can thus create statistics of cloud type occurrence by accumulating the instances at which certain cloud types from active observations coincide with an ROR occurrence (i.e., all cloud type values within the 1° degree grid cell over three months). We can then compare to the contribution of each of 2BCL's seven cloud types (Sc were combined with the rare St) within each ROR to the global fractional occurrence in the last bar of Fig. 9. For example, even if rare in absolute terms, ROR1 proportionally contains ~4 times as many Cb's as the globe as a whole; it also contains ~2.5 times more cirrus and minute amounts of St+Sc compared to the global average. The high proportion of Ns in ROR3 is consistent with its occurrence over the Southern Ocean, where persistent drizzle is common. Anomalously many Cu relative to Sc and their global populations are found in ROR5 corresponding to the aforementioned marine shallow convection mixture. About twice as many St+Sc compared to climatology are encountered in ROR2, while other types occur at rates near or below their global climatology.

Cloud types encountered within RORs at such rates confirm our previous interpretations of their nature.

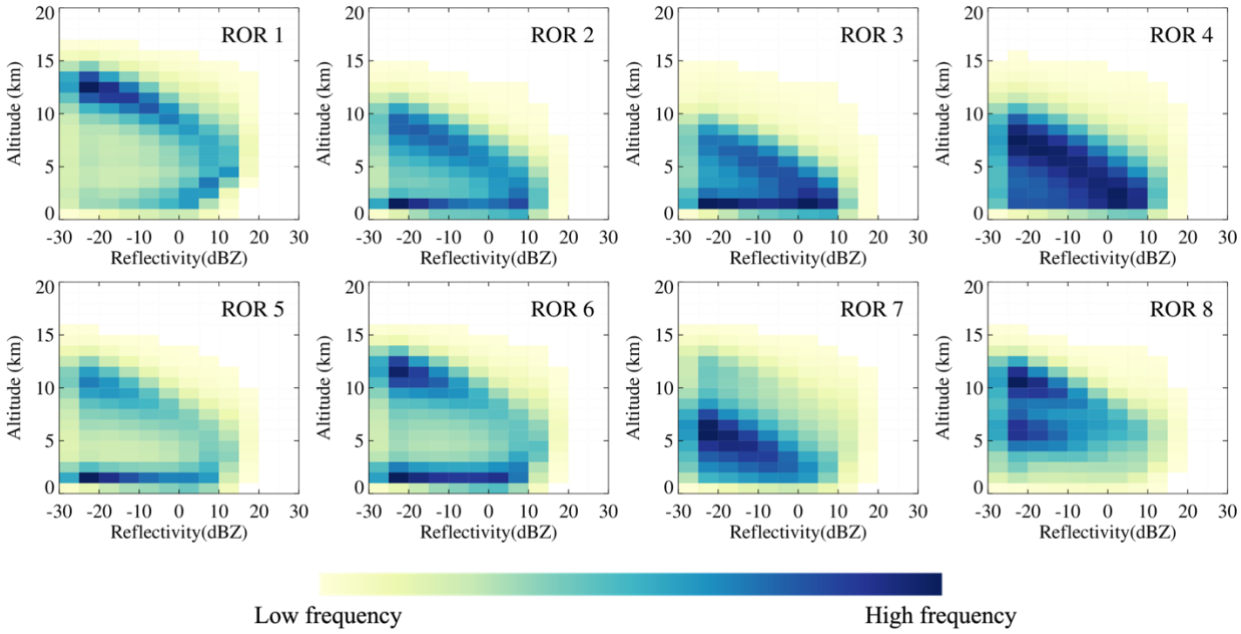

Fig. 10. Composite CFADs for each ROR created by accumulating 2B-GEOPROF R05 reflectivities for the 3-month periods used for ROR assignment in 1° degree grid cells. The frequency normalization (the details of which are irrelevant) is performed separately for each ROR.

To gauge the type and vertical locations of peak occurrence of hydrometeors within RORs, composite CFADs (Contour Frequency by Altitude Diagrams) are constructed from CPR reflectivities (Fig. 10). Our CFADs were created using CloudSat's 2B-GEOPROF.P1 R05 product (Marchand et al. 2008) for the period 2007-2020. The 2B-GEOPROF product identifies those levels in the vertical column sampled by the CPR that contain significant radar echo from hydrometeors (rather than noise or radar clutter) and provides an estimate of the radar reflectivity factor for each of these volumes. CFADs are essentially joint histograms showing the frequency of occurrence of CPR reflectivities within predetermined dBZ bins as a function of height. Each CFAD was normalized separately to the number of observations available for the specific ROR. Frequency peaks at low reflectivity values generally indicate the presence of non-precipitating clouds, while high values above 0 dBZ signify the presence of larger hydrometeors and thus substantial likelihood of precipitation. The atmospheric depth throughout which large reflectivities occur indicates how vertically extensive precipitation is. We see that CFADs provide a perspective consistent with the mixture of CRs RORs are composed of, and their CVS and cloud type makeup previously seen in Figs. 8 and 9. Distinct (separated) high and low cloud layers can be seen in ROR5 and ROR6, while

ROR4 and to a lesser degree ROR3 show vertical development also comprising precipitating parts. The strongest precipitation in the 10-15 dBZ range is unsurprisingly most frequently encountered in the tropical convective ROR1, followed by ROR4 and ROR6.

4. ROR Radiative Impact

We express the radiative impacts associated with RORs in terms of the shortwave (SW) and longwave (LW) cloud radiative effects (CRE) coming from the CERES EBAF dataset (Loeb et al. 2018; Kato et al. 2018). The CERES EBAF product provides a highly stable record of 1° regional, zonal and global monthly mean Top-of-Atmosphere (TOA) and surface (SFC) longwave, and shortwave radiative fluxes, under clear and all-sky conditions. CRE is defined as the difference between all-sky and clear-sky net (down minus up) radiative fluxes at the atmospheric column boundaries (top-of-the-atmosphere TOA and surface SFC).

The CERES EBAF Ed4.2 Level 3b Monthly means dataset we use here contains two versions of gridded clear-sky flux, one coming from cloudless portions of CERES footprints and one meant to resemble the diagnostic clear-sky flux of global models where the properties of the cloud-free version of the grid cell are derived from averaging the non-cloud properties of both the cloud-covered and cloud-free portions of the original (cloudy) grid cell. Since comparison with models does not concern us here, we elect to show results using the more physically defined CREs where the clear-sky flux comes from the former method.

a. Mean ROR radiative effects

Fig. 11a contrasts the (RFO-weighted) SW and LW CRE at the TOA of the various RORs. The CREs of each ROR were calculated by averaging the monthly CERES EBAF CREs of all one-degree grid cells where an ROR is encountered. The comparison aims to distinguish RORs in terms of their contribution to planetary radiative cooling. Indeed, none of the RORs with substantial cloudiness contributes to planetary radiative warming, with ROR7 being the sole ROR where radiative warming (from the LW) and cooling (from the SW) cancel each other nearly perfectly. All other RORs contribute to various degrees to cloud-induced planetary radiative cooling, with the strongest coming from ROR2, the 2nd most frequent ROR which has anomalously high proportions of low clouds and large presence at high latitudes. In this cloudiness mixture, the LW CRE contribution is about 2.5 times smaller than the SW CRE contribution, resulting in a total (=SW+LW) CRE contribution approaching –7 Wm^{-2} which is about a third of the global enhancement of

radiative cooling by clouds (about –20 Wm^{-2}). The next two strongest radiative coolers (ROR3 and ROR5) each contribute about half of the cooling of ROR2, and their almost equal values of total CRE contribution come from very different pairings of RFO-weighted SW and LW CREs.

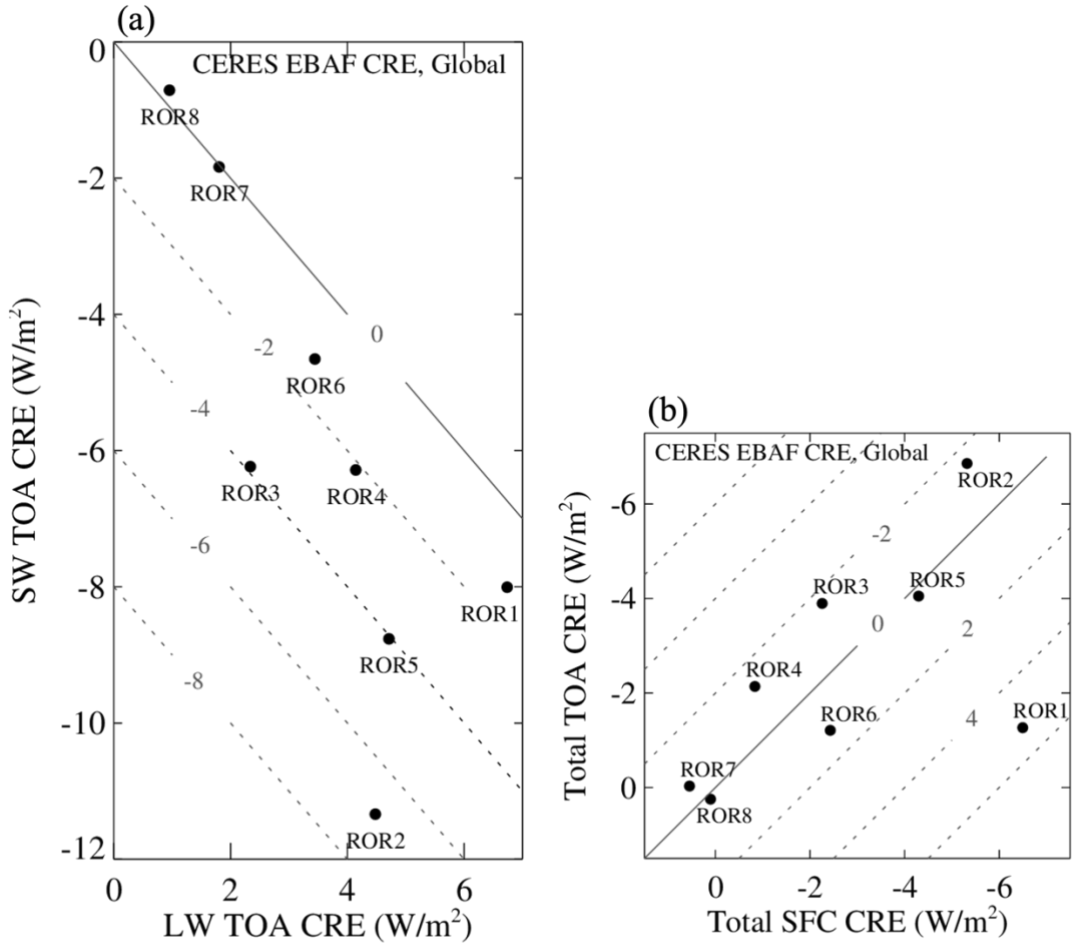

Fig. 11. (a) SW TOA CRE vs LW TOA CRE composited for each ROR from CERES-EBAF; the dashed diagonal lines are isolines of total=SW+LW CRE. (b) Total TOA CRE vs total SFC CRE for each ROR; the dashed diagonal lines are isolines of total atmospheric CRE where positive values indicate that clouds contribute to radiative warming of the atmosphere (vice versa for negative values). All CRE values are weighted by ROR global RFO.

Another cloud radiative impact worth studying is the contribution of RORs to the reduction or enhancement of atmospheric radiative cooling. This is shown in Fig. 11b where the total CRE at TOA and SFC is being contrasted. Isolines of constant atmospheric CRE, the difference between TOA and SFC CRE, are also depicted in the plot, with negative values indicating cloud radiative cooling contributions to the atmosphere, i.e., enhancements of the

clear-sky atmospheric radiative cooling, and isolines of positive values indicating moderating contributions by clouds to the clear-sky radiative cooling. The former effect happens with RORs containing CRs with plentiful low clouds; the atmospheric radiative cooling of (prior versions of) such CRs has indeed been previously shown in Oreopoulos et al. (2016) and Oreopoulos (2022). Three RORs, ROR2, ROR3, and ROR4, contribute nearly equal amounts of about -2 Wm^{-2} additional radiative cooling to the atmosphere. The RORs containing anomalously high proportions of CRs with plentiful high clouds are found to the right of the neutral diagonal; the atmospheric radiative warming effects of (prior versions of) such CRs were also previously recognized in Oreopoulos et al. (2016) and Oreopoulos (2022). The reduction of clear-sky atmospheric radiative cooling, i.e., the warming contribution, is dominated by the predominantly tropical ROR1 encompassing the largest combined amount of stand-alone high and deep convection clouds.

b. CRE Trends

With 20 years of ROR and associated CRE data, we can examine whether any CRE trends (anomalies) can be traced to changes in the properties of specific RORs. Changes in RORs can be viewed as the contribution of two main types of changes: anomalies in ROR populations, namely anomalies relative to the 20-year climatological mean of the ROR RFO, and "internal" anomalies in ROR properties that affect their inherent CRE. We can broadly refer to these as CRE anomalies as "across" and "within" ROR changes, respectively. For the latter category, the major changes in clouds that constitute an ROR are changes in cloud optical thickness, cloud top height, cloud amount (fraction), and changes in cloudless skies within RORs.

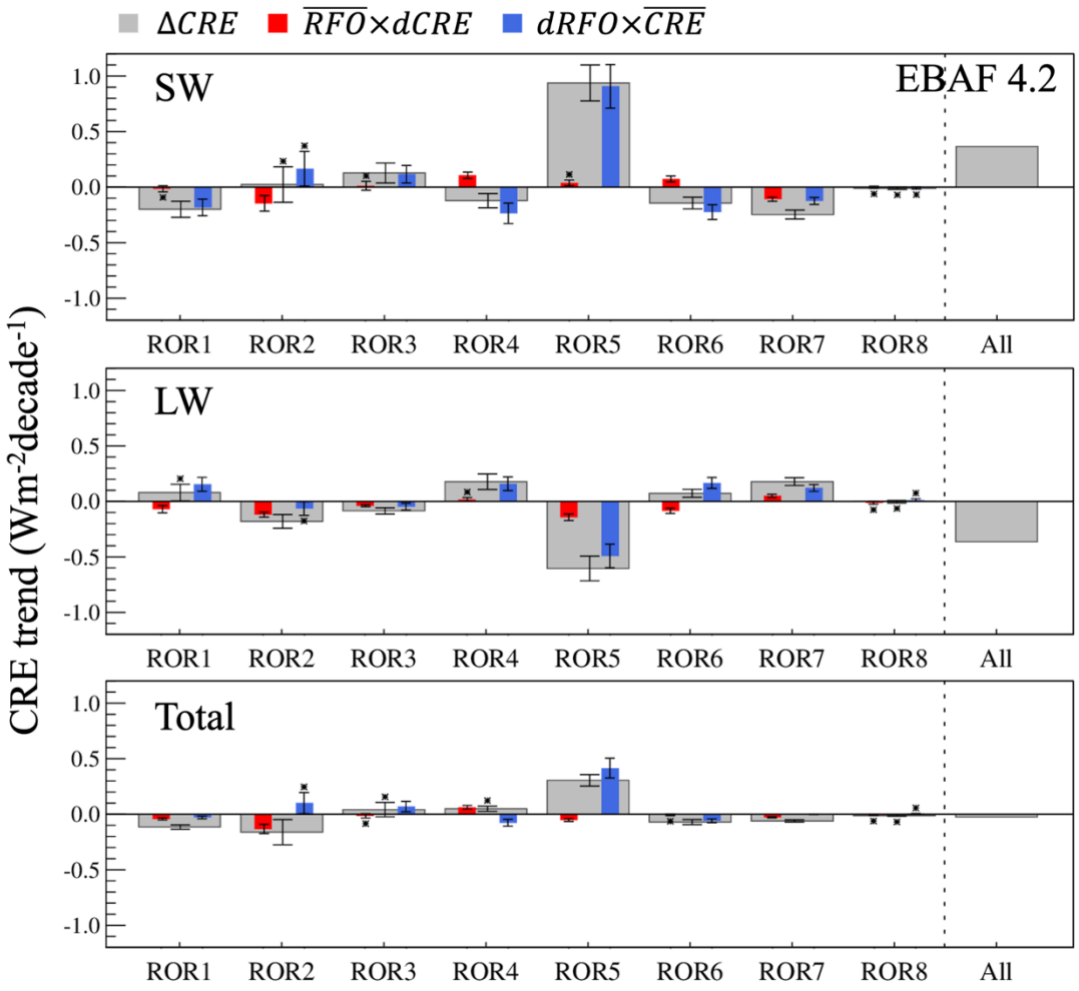

Fig. 12. Trend values (slopes of lines obtained by linearly regressing CRE anomalies against time) expressed as $Wm^{-2}decade^{-1}$ for each ROR's CRE anomaly component, namely, CRE anomaly due to internal changes ("within" RORs, red) CRE anomaly, and CRE anomaly due to RFO changes ("across" RORs, blue); a smaller third term, the covariance term, is not shown. The broad gray bars are the sum of the three components, i.e., the overall CRE trend for each ROR. Top panel is for SW CRE, middle panel is for LW CRE, and bottom panel is for total=SW+LW CRE. The asterisk indicates statistical insignificance per an F-test. The error bars represent 1.96 times the standard error (95% confidence level) of the slope of the linear fit calculated from eq. (1).

Following previous decompositions of observables assigned to CRs (e.g., Tan et al. 2015; Zelinka et al. 2023; Jin et al. 2023), the CRE anomaly/trend of each ROR is decomposed into a within, an across, and a covariance term. Fig. 12 shows the 20-year trends of the first two (largest) terms, expressed as $Wm^{-2}decade^{-1}$, of each ROR's SW, LW and total TOA CRE. The within-ROR term (red bars) is calculated by multiplying the global multi-annual mean RFO of the ROR with the trend, from linear regression versus time, of monthly CRE anomalies with respect to the multi-annual CRE monthly means for that ROR. Similarly, the across-ROR term (blue bars) is calculated by multiplying the global mean ROR CRE with the

ROR's RFO trend calculated from regressing monthly RFO anomalies versus time. The gray bars show the CRE trends of each ROR calculated directly by regressing the monthly CRE anomalies of that ROR versus time; we confirmed that the sum of the three trends from decomposition (including the covariance term not shown) match the directly calculated CRE trend. We have also verified that adding the individual ROR total CRE trends (rightmost gray bar) yields global LW and SW CRE trends that largely agree with Raghuraman et al. (2023), namely opposing 0.36 $Wm^{-2}decade^{-1}$ trends (warming for SW and cooling for LW). Overlayed on each bar of Fig. 12 is the 1.96×standard error (S.E) (representing the 95% confidence level) of the linear regression's slope, calculated from Eq. (1), as a measure of its uncertainty.

$$S.E = \frac{\sqrt{\frac{\sum_{i=1}^{N}(y_i - \hat{y}_i)^2}{N'}}}{\sqrt{\sum_{i=1}^{N}(x_i - \bar{x})^2}} \quad (1)$$

where N' represents the ROR-specific degrees of freedom, $\hat{y}_i$ represents the estimated *y* value from the linear fit, and $\bar{x}$ is the mean value of the *x* variable. Here, CRE anomalies correspond to the *y* variable, while for *x*, we use normalized time (fraction of decade) ranging from 0 to 2, to represent 20 years in monthly increments (~0.004 in the normalized scale). The asterisk above or below the bars mark the trends for which we cannot reject at the 95% confidence level the null hypothesis of zero correlation between CRE anomalies and time; in other words, these CRE trends are statistically insignificant at the 95% level.

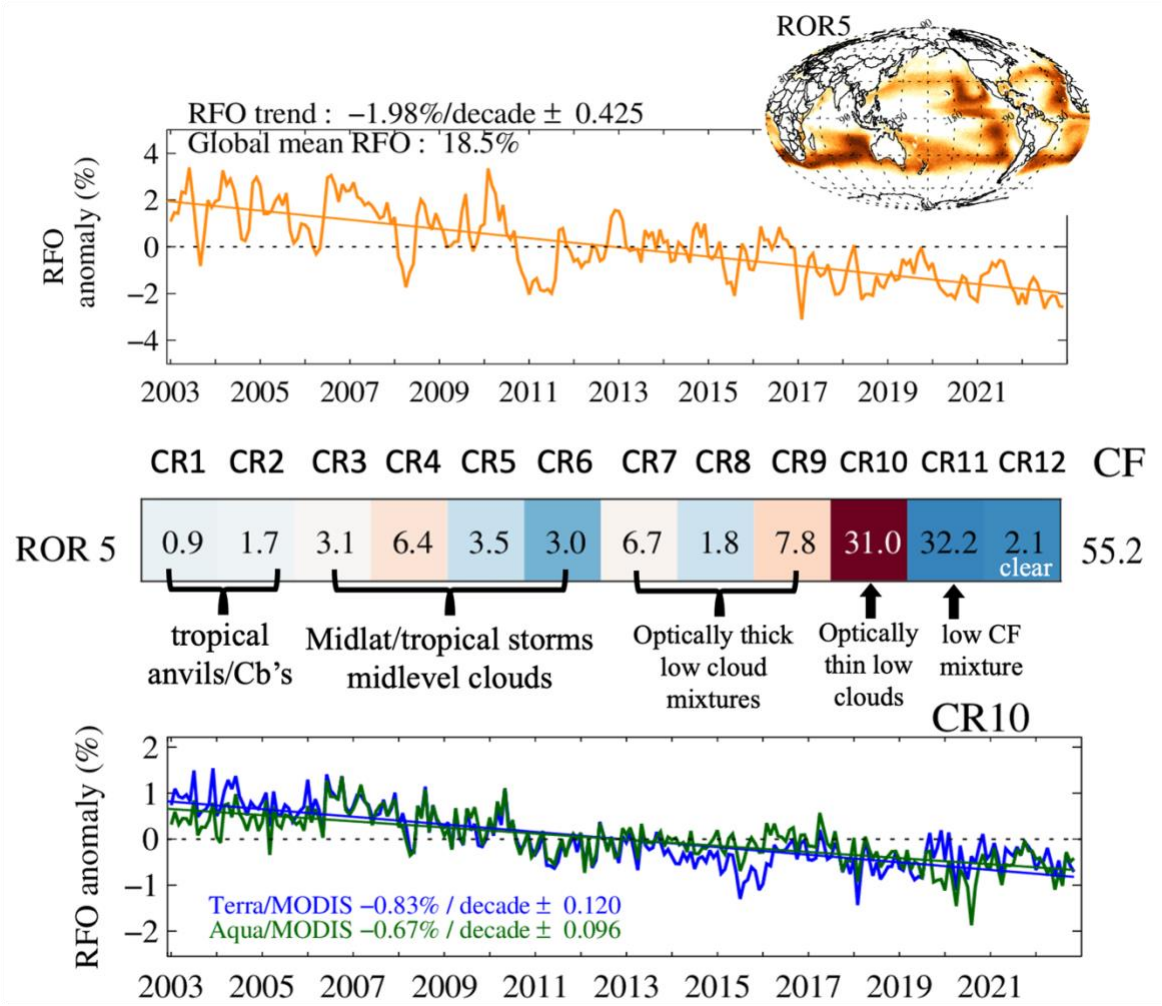

Fig. 13. Interpretation of ROR5 RFO trend in terms of CR10 RFO trend. The top panel shows the ROR5 RFO anomaly time series and trend line fit, while the bottom panel shows CR10 RFO anomaly time series (and trend line fits) separately for Terra and Aqua CR10s. The middle panel shows the ROR5 centroid.

The biggest CRE anomaly is associated with ROR5 and is due to RFO anomalies (large blue bar in Fig. 12). The time series of ROR5 RFO anomaly is shown in the top panel of Fig. 13. A negative trend in ROR5 RFO is consistent with a weakening of both the SW CRE (less negative values) and the LW CRE (smaller positive values). ROR5 contains large amounts of CR10, as shown in the middle panel of Fig. 13, which was previously found in Cho et al. (2021) to exhibit a decreasing populations over approximately the same period examined here (an updated CR10 RFO anomaly time series is shown in the bottom panel of Fig. 13). We thus attribute ROR5's RFO decrease to CR10's RFO decrease, i.e., a decrease in the population of cloud mixtures dominated by shallow convection (Cho et al. 2021).

c. CRE feedback

In addition to ROR CRE trends, we also calculate ROR "CRE feedback" (Jin et al. 2023) (strictly not the "cloud feedback" which accounts for only cloud changes while everything else remains constant), using the same framework as above, namely decomposing each ROR's CRE feedback in terms of within-ROR and across-ROR components, similarly to Jin et al. (2023). Instead of linearly regressing CRE and RFO monthly anomalies against time as in the CRE trend analysis of the previous subsection, we now regress these anomalies against the global monthly surface skin temperature (T_s) anomalies of MERRA-2. We present two versions of CRE feedback, one where we ignore ENSO effects on the T_s anomaly (left panels) and one where the ENSO effects on T_s are removed (right panels) by using the T_s anomaly residuals from the linear regression of T_s anomalies against the Niño-3.4 index, as in Jin et al. (2023). Results for both versions of the CRE feedback are shown in Fig. 14 where gray bars, blue bars, red bars, and asterisks have the same meaning as in Fig. 12 (but now for CRE feedback). The error bars once again come from Eq. (1) with x representing the T_s anomaly for the left panels, and the T_s anomaly adjusted for ENSO effects in the right panels.

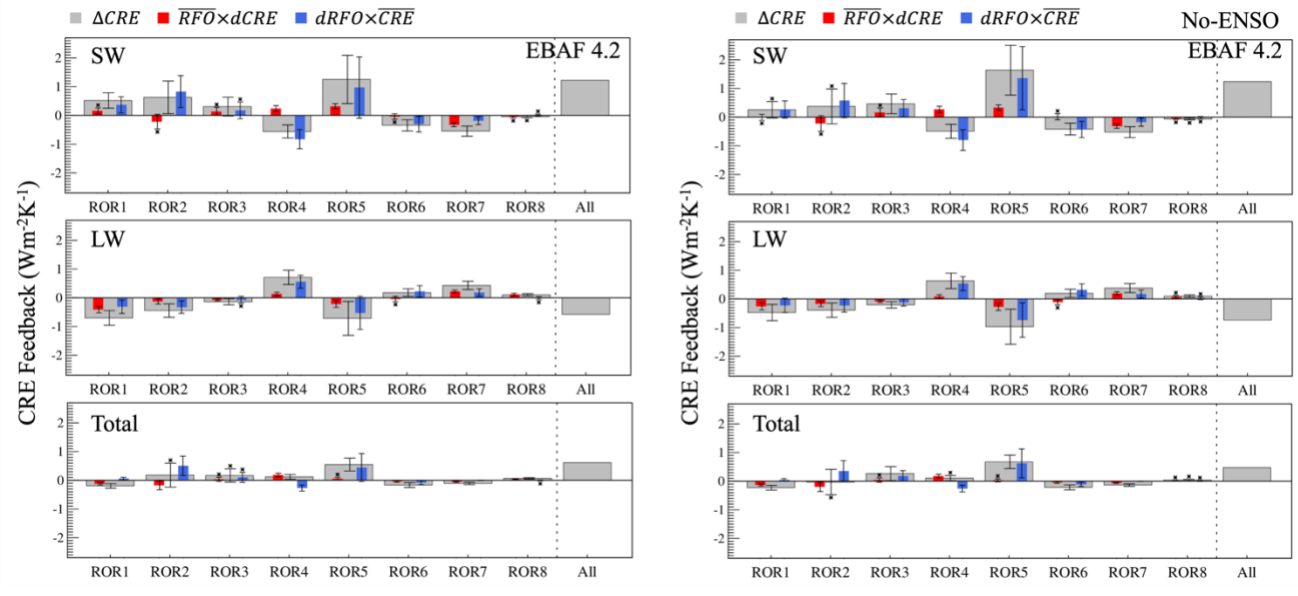

Fig. 14. CRE feedback values (slopes of lines when linearly regressing CRE anomalies against T_s anomalies) expressed as $Wm^{-2}K^{-1}$ for the two major ROR CRE anomaly components (red and blue bars), and for the overall CRE anomaly (gray bars), as in Figure 12. The CRE feedback on the right panel has ENSO effects on the T_s anomalies removed.

The CRE feedback results mirror the CRE trend results indicating positive monthly T_s anomalies for the period of analysis, i.e., a positive trend of T_s with time. Removing the ENSO effect has a notable impact on the CRE feedback of ROR5, which becomes stronger by ~23% overall, indicating a considerable masking effect of ENSO on the feedback of ROR5 clouds. This SW masking effect was previously noted by Jin et al. (2023) during the

DJF season for the SW CRE feedback of their optically thin low cloud regime which roughly corresponds to ROR5 containing plentiful Cho et al. (2021) CR10, as shown earlier. Jin et al. (2023) also noticed that for the same season ENSO amplifies "true" SW CRE feedback for optically thick low clouds. In accordance, we see a reduction in the SW CRE feedback of ROR2, containing high amounts of Cho et al, (2021) CR8 and CR9, when effects of ENSO on T_s are removed.

The overall global CRE feedback over our 20-year period when adding ROR feedbacks (sum of grey bars) is 1.2 $Wm^{-2}K^{-1}$ for SW and −0.6 $Wm^{-2}K^{-1}$ for LW as depicted by the rightmost gray bar of each panel in Fig. 14. The global CRE feedback values are comparable to several studies using observed clouds and radiation; Raghuraman et al. (2023) found 0.80 ± 0.52 $Wm^{-2}K^{-1}$ for SW and −0.57 ± 0.34 $Wm^{-2}K^{-1}$ for LW tropical (30°S - 30°N) cloud feedback, while Chao et al. (2024) found 0.57 ± 0.27 $Wm^{-2}K^{-1}$ for total (LW+SW) cloud feedback. Note that both Raghuraman et al. (2023) and Chao et al. (2024) calculate the cloud feedback adjusted for non-cloud effects, rather than the CRE (difference between all-sky and clear-sky radiative fluxes) feedback as we do. It is quite possible that changes in cloudless skies have a non-negligible contribution to CRE feedback.

5. Discussion and conclusions

This work introduces the concept of Regimes of Regimes (RORs) as a viable option for effectively capturing the main modes of global cloudiness on monthly/seasonal scales. RORs are higher-order cloud classifications describing how semi-instantaneous mesoscale cloud variability is organized at these temporal scales, while also preserving information on cloud opacity and height co-variability at the instrument footprint level as encoded in joint histograms of cloud populations within certain combinations of CTP and COT. RORs thus provide an objective way for identifying areas and times of interest for specific types of cloudiness without relying on arbitrary criteria for region selection. The physical meaningfulness of RORs is supported by the cohesive spatial patterns in which they are organized as well as the emergence of prevalent areas of occurrence over the full 20-year period under examination. Their organization corresponds quite well to distinct dynamical regimes and atmospheric circulation features. Further confirmation of the systematic makeup of the RORs is obtained by examining composites of cloud products from active observations containing information about hydrometeor vertical profiles. Additionally, RORs can be more easily combined with other high-level datasets (Level-3b or Level-4), such as CERES EBAF,

577 monthly precipitation data (e.g., GPCP or IMERG) and climate indices (e.g., Niño-3.4 index),
578 which are incompatible with daily CRs.

579 When paired with radiation data from the CERES EBAF dataset, RORs reveal which
580 cloud systems are most responsible for planetary radiative cooling (ROR2, the 2nd most
581 frequent ROR with high proportions of high latitude low clouds) and counteracting (tropical
582 ROR1 with plentiful high clouds) or enhancing (three low cloud RORs) atmospheric clear-
583 sky radiative cooling. They also reveal what kinds of cloud mixtures contribute the most to
584 LW and SW CRE trends and feedbacks. We find that the ROR containing frequent
585 occurrences of shallow convection (ROR5) has been becoming progressively rarer because
586 the CR that captures the shallow convection has also experienced a shrinking population. In
587 other words, the fact that shallow convection has been decreasing in the last 20 years can now
588 be seen not only in cloud regimes dominated by such clouds, but also in even broader cloud
589 mixtures with other cloud regimes. It appears that contributions to CRE trends from internal
590 changes in the properties of RORs (i.e, "within" ROR changes due to variations in their
591 extent, optical depth, altitude, and the environment they are embedded in) are substantially
592 weaker. Larger internal changes in the CRs themselves may still be taking place, but they can
593 be conceivably compensated by changes within the other CRs that the ROR encompasses,
594 i.e., across CR changes within the ROR (although this remains to be shown).

595 We have also examined the feasibility of producing RORs in an Earth System Model,
596 specifically NASA's GEOS model (Rienecker et al. 2008). We have confirmed that it is
597 indeed possible and actually quite trivial to generate RORs, but leave this analysis for a
598 separate study. Here we only briefly describe how this can be accomplished. What makes
599 derivation of RORs in climate models possible is the capability of classifying model clouds
600 according to observed CRs (Williams and Webb 2009) thanks to subgrid cloudiness
601 expressed in terms of the aforementioned CTP-COT joint histograms (JHs). Such JHs can be
602 produced by COSP's ISCCP and MODIS simulators (Bodas-Salcedo et al. 2011). The
603 model's CR occurrences are generated by assigning the model JH to the closest observed CR
604 (Williams and Webb 2009), rather than performing new clustering on the model's JH as has
605 been suggested earlier by Williams and Tselioudis (2007). Once a model's cloudiness is
606 expressed in terms of CRs, RORs can also be produced. There are two avenues to accomplish
607 this. One is to perform clustering of the CR frequency of occurrence (FOC) histograms, as in
608 observations. Another is to compare the model's CR FOC histograms to the centroids of the

observed RORs, and assign the model histogram to the ROR with the closest matching centroid.

The overall philosophy of clustering occurrences of distinct cloud classes over a period of time to create a higher-level classification that conveys how they mix can be broadened to combine datasets of different provenance. For example, one could attempt to cluster FOC histograms of spatiotemporally matched classes of passive and active origin, or of combined FOC histograms of MODIS CRs (Cho et al. 2021) and ISCCP WSs (Tselioudis et al. 2021). We propose that the utility of the broad concept of clustering FOC histograms of different (co-varying) cloud properties, cloud mixtures, or other cloud entities continues to be explored in future work. Novel ways of organizing (and effectively compressing) cloud information can be potentially as useful for understanding climatic trends as the fundamental understanding of cloud processes and patterns at high resolutions.

Acknowledgments.

Resources supporting this work were provided by the NASA High-End Computing (HEC) Program through the NASA Center for Climate Simulation (NCCS) at Goddard Space Flight Center. Support by NASA's CloudSat-CALIPSO Science Team and MEaSUREs programs is gratefully acknowledged.

Data Availability Statement.

MODIS equal-angle daily CRs are available at https://doi.org/10.5067/MEASURES/MODISCR/EQANGD/DATA301, MODIS RORs are available at https://doi.org/10.5281/zenodo.11099765. The Clustering code used to derive the ROR can be found at https://doi.org/10.5281/zenodo.13351479. The 2B-CLDCLASS-LIDAR and 2B-GEOPROF datasets are available at http:// www.cloudsat.cira.colostate.edu/ and CERES EBAF Level 3b dataset is available at https://ceres.larc.nasa.gov/data/. The Surface Skin Temperature (T_s) and omega at 500 hPa from MERRA-2 are available at https://goldsmr4.gesdisc.eosdis.nasa.gov/data/MERRA2/M2T1NXSLV.5.12.4/

REFERENCES

639 Bankert, R. L., 1994: Cloud classification of AVHRR imagery in maritime regions using a
640 probabilistic neural network. *J. Appl. Meteor.*, **33**, 909-918.

641 Bodas-Salcedo, A., Webb, M.J., Bony, S., Chepfer, H., Dufresne, J.L., Klein, S.A., Zhang,
642 Y., Marchand, R., Haynes, J.M., Pincus, R. and John, V.O., 2011: COSP: Satellite
643 simulation software for model assessment. Bulletin of the American Meteorological
644 Society, 92(8), pp.1023-1043.

645 Boucher, O., D. Randall, P. Artaxo, C. Bretherton, G. Feingold, P. Forster, V.-M. Kerminen,
646 Y. Kondo, H. Liao, U. Lohmann, P. Rasch, S.K. Satheesh, S. Sherwood, B. Stevens and
647 X.Y. Zhang, 2013: Clouds and Aerosols. In: Climate Change 2013: The Physical Science
648 Basis. Contribution of Working Group I to the Fifth Assessment Report of the
649 Intergovernmental Panel on Climate Change [Stocker, T.F., D. Qin, G.-K. Plattner, M.
650 Tignor, S.K. Allen, J. Boschung, A. Nauels, Y. Xia, V. Bex and P.M. Midgley (eds.)].
651 Cambridge University Press, Cambridge, United Kingdom and New York, NY, USA.

652 Ceccaldi, M., J. Delanoë, R. J. Hogan, N. L. Pounder, A. Protat, and J. Pelon, 2013: From
653 CloudSat-CALIPSO to EarthCare: Evolution of the DARDAR cloud classification and its
654 comparison to airborne radar-lidar observations, J. Geophys.Res. Atmos., 118, 7962–
655 7981, doi:10.1002/jgrd.50579.

656 Chao, L.-W., Zelinka, M. D., & Dessler, A. E. 2024: Evaluating cloud feedback components
657 in observations and their representation in climate models. Journal of Geophysical
658 Research: Atmospheres, 129, e2023JD039427. https://doi.org/10.1029/2023JD039427

659 Cho, N., Tan, J. and Oreopoulos, L., 2021: Classifying planetary cloudiness with an updated
660 set of MODIS cloud regimes. *Journal of Applied Meteorology and Climatology*, *60*(7),
661 pp.981-997.

662 Davies, D. L., and D. W. Bouldin, 1979: A cluster separation measure. IEEE Trans. Pattern
663 Anal. Mach. Intell., PAMI-1, 224–227, https://doi.org/10.1109/TPAMI.1979.4766909.

664 Gelaro, R., and Coauthors, 2017: The Modern-Era Retrospective Analysis for Research and
665 Applications, version 2 (MERRA-2). J. Climate, 30, 5419–5454,
666 https://doi.org/10.1175/JCLI-D-16-0758.1

667 Jakob, C., and G. Tselioudis, 2003: Objective identification of cloud regimes in the tropical
668 western Pacific. Geophys. Res. Lett., 30, 2082, https://doi.org/10.1029/2003GL018367.

669 Jin, D., L. Oreopoulos, D. Lee and N. Cho, 2021: Cloud-precipitation hy- brid regimes and
670 their projection onto IMERG precipitation data. J. Appl. Meteor. Climatol., 60, 733–748,
671 https://doi.org/ 10.1175/JAMC-D-20-0253.1.

672 Jin, D., R. J. Kramer, L. Oreopoulos, and D. Lee, 2023: ENSO Disrupts Boreal Winter CRE
673 Feedback. *J. Climate*, **37**, 585–603, https://doi.org/10.1175/JCLI-D-23-0282.1.

674 Kato, S., F. G. Rose, D. A. Rutan, T. E. Thorsen, N. G. Loeb, D. R. Doelling, X. Huang, W.
675 L. Smith, W. Su, and S.-H. Ham, 2018: Surface irradiances of Edition 4.0 Clouds and the
676 Earth's Radiant Energy System (CERES) Energy Balanced and Filled (EBAF) data
677 product, *J. Climate*, **31**, 4501-4527, doi: 10.1175/JCLI-D-17-0523.1.

678 Koren, I., Oreopoulos, L., Feingold, G., Remer, L. A., and Altaratz, O.: How small is a small
679 cloud?, Atmos. Chem. Phys., 8, 3855–3864, https://doi.org/10.5194/acp-8-3855-2008,
680 2008.

681 Loeb, N.G., Doelling, D.R., Wang, H., Su, W., Nguyen, C., Corbett, J.G., Liang, L.,
682 Mitrescu, C., Rose, F.G. and Kato, S., 2018: Clouds and the earth's radiant energy system
683 (CERES) energy balanced and filled (EBAF) top-of-atmosphere (TOA) edition-4.0 data
684 product. *Journal of Climate*, *31*(2), pp.895-918.

685 Marchand, R., G.G. Mace, T. Ackerman, and G. Stephens, 2008: Hydrometeor Detection
686 Using Cloudsat—An Earth-Orbiting 94-GHz Cloud Radar. J. Atmos. Oceanic Technol.,
687 25, 519–533.

688 McDonald, A. J., J. J. Cassano, B. Jolly, S. Parsons, and A. Schuddeboom, 2016: An
689 automated satellite cloud classification scheme using self- organizing maps: Alternative
690 ISCCP weather states. J. Geophys. Res., 121, 13 009–13 030,
691 https://doi.org/10.1002/2016JD025199.

692 Oreopoulos L., N. Cho, D. Lee, et al. 2014 : An examination of the nature of global MODIS
693 cloud regimes. *Journal of Geophysical Research: Atmospheres* 119 (13): 8362-8383
694 [10.1002/2013JD021409]

695 Oreopoulos, L., Cho, N. and Lee, D., 2017: New insights about cloud vertical structure from
696 CloudSat and CALIPSO observations. *Journal of Geophysical Research:*
697 *Atmospheres*, *122*(17), pp.9280-9300.

Oreopoulos, L., Cho, N., Lee, D. and Kato, S., 2016: Radiative effects of global MODIS cloud regimes. *Journal of Geophysical Research: Atmospheres*, *121*(5), pp.2299-2317.

Oreopoulos, L., 2022: Understanding Global Cloud Radiative Impacts. *Studies Of Cloud, Convection And Precipitation Processes Using Satellite Observations*, *3*, p.129.

Raghuraman, S. P., D. Paynter, R. Menzel, and V. Ramaswamy, 2023: Forcing, Cloud Feedbacks, Cloud Masking, and Internal Variability in the Cloud Radiative Effect Satellite Record. *J. Climate*, **36**, 4151–4167, https://doi.org/10.1175/JCLI-D-22-0555.1.

Rienecker, M. M., Suarez, M. J., Todling R., Bacmeister J., Takacs L., Liu H.-C., Gu W., Sienkiewicz M., Koster, R. D., Gelaro, R., Stajner, I., and Nielsen, J. E. 2008: The GEOS-5 Data Assimila- tion System Documentation of Versions 1 5.0.1, 5.1.0, and 5.2.0. NASA/TM–2008–2 104606, Vol. 27, 118 pp.

Rossow, W.B., and R.A. Schiffer, 1999: Advances in understanding clouds from ISCCP. *Bull. Amer. Meteorol. Soc.*, **80**, 2261-2288, doi:10.1175/1520 0477(1999)080<2261:AIUCFI>2.0.CO;2.

Rossow, W., G. Tselioudis, A. Polak, and C. Jakob, 2005 : Tropical climate described as a distribution of weather states indicated by distinct mesoscale cloud property mixtures, *Geophys. Res. Lett.*, 32, L21812, doi:10.1029/2005GL024584.

Sassen, K., Wang, Z. and Liu, D., 2008: Global distribution of cirrus clouds from CloudSat/Cloud-Aerosol lidar and infrared pathfinder satellite observations (CALIPSO) measurements. *Journal of Geophysical Research: Atmospheres*, *113*(D8).

Schuddeboom, A., A. J. McDonald, O. Morgenstern, M. Harvey, and S. Parsons, 2018: Regional regime-based evaluation of present-day general circulation model cloud simulations using self-organizing maps. J. Geophys. Res., 123, 4259–4272, https:// doi.org/10.1002/2017JD028196.

Tan, J., Jakob, C., Rossow, W. and Tselioudis, G., 2015: Increases in tropical rainfall driven by changes in frequency of organized deep convection. Nature 519, 451– 454 (2015). https://doi.org/10.1038/nature14339

Tselioudis, G. and Rossow, W.B., 2011: Time scales of variability of the tropical atmosphere derived from cloud-defined weather states. *Journal of Climate*, *24*(3), pp.602-608.

Tselioudis, G., W. Rossow, Y. Zhang, and D. Konsta, 2013: Global weather states and their properties from passive and active satellite cloud retrievals. J. Climate, 26, 7734–7746, https:// doi.org/10.1175/JCLI-D-13-00024.1.

Tselioudis, G., Rossow, W.B., Jakob, C., Remillard, J., Tropf, D. and Zhang, Y., 2021: Evaluation of clouds, radiation, and precipitation in CMIP6 models using global weather states derived from ISCCP-H cloud property data. Journal of Climate, 34(17), pp.7311-7324.

Wang, Z. and K. Sassen, 2001: Cloud type and macrophysical property retrieval using multiple remote sensors. *J. Appl. Meteor*., **40**, 1665-1682.

Welch, R. M., S. K. Sengupta, A. K. Goroch, P. Rabindra, N. Rangaraj, and M. S. Navar, 1992: Polar cloud and surface classification using AVHRR imagery: An intercomparison of methods. *J. Appl. Meteor.*, **31**, 405-420.

World Meteorological Organization, 1956: *International Cloud Atlas: abridged atlas.* WMO, Geneva [c1969].

Williams, K.D. and Tselioudis, G., 2007: GCM intercomparison of global cloud regimes: Present-day evaluation and climate change response. *Climate Dynamics*, *29*, pp.231-250.

Williams, K.D. and Webb, M.J., 2009: A quantitative performance assessment of cloud regimes in climate models. *Climate dynamics*, *33*, pp.141-157.

Zelinka, M.D., Tan, I., Oreopoulos, L. and Tselioudis, G., 2023: Detailing cloud property feedbacks with a regime-based decomposition. *Climate Dynamics*, *60*(9-10), pp.2983-3003.